Journal of
Materials Chemistry A

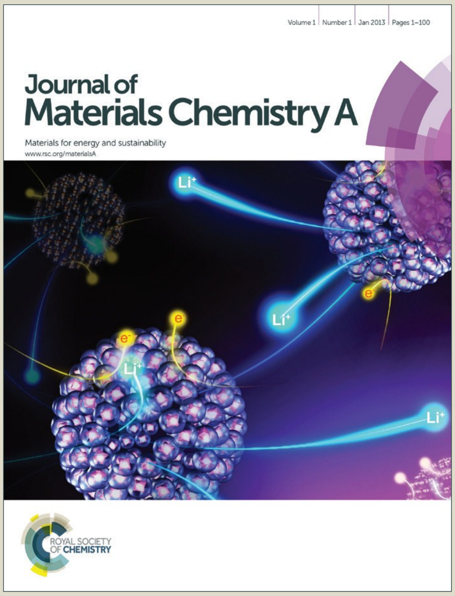

www.rsc.org/materialsA

Journal Name

ARTICLE

Low Cost Flexible 3-D Aligned and Cross-linked Efficient $ZnFe_2O_4$ Nano-flakes Electrode on Stainless Steel Mesh for Asymmetric Supercapacitor

Received 00th January 20xx,
Accepted 00th January 20xx

DOI: 10.1039/x0xx00000x

www.rsc.org/

Madagonda M. Vadiyar,[a] Sagar C. Bhise,[a] Sanjay S. Kolekar,[a]* Jia-Yaw Chang,[b]* Kaustubh S. Ghule[c] and Anil V. Ghule[c]*

Simple and economic approach for the growth of 3-D aligned and cross-linked $ZnFe_2O_4$ nano-flakes on flexible stainless steel mesh (FSSM) substrate (300 mesh) using rotational chemical bath deposition technique for fabricating efficient asymmetric supercapacitor is reported. The prepared $ZnFe_2O_4$ nano-flake thin film ($ZnFe_2O_4$/FSSM-300) as anode in combination with $Ni(OH)_2$/FSSM-300 as cathode is used as asymmetric supercapacitor. Furthermore, $ZnFe_2O_4$ nano-flakes were also grown on FSSM with different mesh and designated as $ZnFe_2O_4$/FSSM-200, $ZnFe_2O_4$/FSSM-250 and $ZnFe_2O_4$/FSSM-300, respectively for investigating the effect of mesh size on the formation morphology and their electrochemical performance. Amongst the samples, $ZnFe_2O_4$/FSSM-300 exhibited excellent supercapacitive property like higher specific capacitance (1625 F g^{-1} at 1 mA cm^{-2}) and excellent cycle stability (8000 cycles, 97% retention), which is marginally higher than $ZnFe_2O_4$/FSSM-250 (545 F g^{-1} at 1 mA cm^{-2}, 70% retention), $ZnFe_2O_4$/FSSM-200 (241 F g^{-1} at 1 mA cm^{-2}, 56% retention) and for other earlier reported ferrites. In addition, the fabricated asymmetric pseudocapacitor device delivered better performance with high specific capacitance (118 F g^{-1} at 5 mA cm^{-2}), excellent cycle stability (8000 cycles, 83 % capacitance retention) and high energy density (42 Wh kg^{-1}) even at higher power density (5 kW kg^{-1}).

1. Introduction

The rapid depletion of fossil fuels,[1] increase in environmental pollution and elevating global warming issues[2] have poised the urgent need for the development of new alternative and economic renewable energy sources and technologies associated with energy storage and conversion.[3] In recent years, the maximum utilization of portable electronic devices[4] and hybrid vehicles[5] has created a seemingly insatiable demand for energy storage, which has also presented great challenges towards the enhancement of electrochemical performance.[6] In these context, energy storage devices such as supercapacitors (SCs)[7] and lithium ion batteries[8, 9] have a great attention to alleviate the energy crisis. Amongst the energy storage devices, SCs have attracted more attention as promising energy storage device because of their properties like high power density, long cycle stability, higher specific capacitances and fast charging-discharging rate etc.[10, 11] SCs are classified into electric double layer capacitors (EDLCs) and pseudocapacitors based on their energy storage mechanisms.[12, 13] In EDLCs, the energy is stored with charge accumulation at electrode-electrolyte interface.[14] Particularly, carbon based materials such as activated carbon; carbon nanotubes (CNT), graphene oxide, graphene etc. are explored as electrode materials for EDLCs.[15-17] While in pseudocapacitors, the energy storage is *via* pair of Faradays redox reactions at electrode surface.[18] The transition metal oxides with binary (MnO_2, Mn_3O_4, Fe_3O_4, Co_3O_4, CeO_2, Fe_2O_3, RuO_2 and WO_3)[19-24] and ternary ($NiCo_2O_4$, $ZnCo_2O_4$, $CoFe_2O_4$, $NiFe_2O_4$, $CuFe_2O_4$ and $ZnFe_2O_4$)[25-27] compositions are being studied and explored as promising electrodes for pseudocapacitors, because of their properties such as high specific capacitance, longer life stability and environmental benignity. Amongst the transition metal oxides, metal ferrite (MFe_2O_4, where M refers to divalent metal ions) with spinel structure based electrodes are amongst the most studied candidates in SCs due to their excellent redox behaviour demonstrated by Fe element. Among the metal ferrites, $ZnFe_2O_4$ is one of the promising anode materials for pseudocapacitors considering its important inherent features like low cost, non-toxic nature, abundance, easy availability of metal salts, excellent redox behaviour, high surface area, high thermal stability etc.[28]

From the literature reports, it is observed that the utility of SCs so far, have been hampered as a result of the limitation posed by the energy density issue.[29,30] Thus, to circumvent this issue, extensive research efforts are put together by scientists and technologists all around the world. Literature survey has revealed that the energy density mainly depends on the materials, nanostructures, architecture of the electrodes and types of electrolytes employed.[31,]

---

[a] *Analytical Chemistry and Material Science Research Laboratory, Department of Chemistry, Shivaji University, Kolhapur 416004, Maharashtra, India. E-mail: sskolekar@gmail.com*

[b] *Department of Chemical Engineering, National Taiwan University of Science and Technology, Taipei 10607, Taiwan E-mail: jychang@mail.ntust.edu.tw*

[c] *Green Nanotechnology Laboratory, Department of Chemistry, Shivaji University, Kolhapur 416004, Maharashtra, India. E-mail: anighule@gmail.com*

† *Footnotes relating to the title and/or authors should appear here.*

Electronic Supplementary Information (ESI) available: [details of any supplementary information available should be included here]. See DOI: 10.1039/x0xx00000x

[32] Thus, in this context, the researchers have focused their major attention on the tailoring and nanostructuring of electrode material and the use of appropriate electrolytes. As a result, various synthetic methods such as chemical vapor deposition (CVD), sputtering, molecular beam epitaxy, hydrothermal, chemical bath deposition (CBD), sol-gel, solvothermal, ultrasonication, screen printing, spray pyrolysis, spin coating etc.[33-35] are being explored with great interest for fabricating thin film based electrode materials with different nanostructures like nanorods, nanotubes, nanocrystals, nano-flower, nano-flakes, nano-spheres and nano-grains.[36, 37] In thin film preparation, the material is directly deposited onto the conducting substrates like carbon cloth, Ni foam, graphite sheets, Cu foil, Ti foil and stainless steel without using binders, wherein, electrodeposition, CVD or vacuum deposition techniques are preferred choices.[38, 39] Furthermore, high cost and toxicity concerns in substrates like carbon cloth, Ni foam, Cu foil, Ti foil etc. are the limiting factors.[40] Thus, substrates like stainless steel plates are among the most explored substrates due to their low cost, less toxicity, rough surface and easy available in the market. Very recently, flexible stainless steel mesh (FSSM) substrates are being explored with great interest,[41] most in which, electrodeposition and vacuum deposition techniques are reported for the growth of the material thin films,[42] with inherent limitation and difficulties of large scale and large area deposition.

With this motivation, to address some of these limiting factors, herein this work, we report the synthesis of 3-D aligned and cross-linked $ZnFe_2O_4$ nano-flakes on low cost flexible stainless steel mesh (FSSM) for the first time by employing rotational chemical bath deposition method (R-CBD) having potential for economically depositing the material on large scale and large area for developing efficient supercapacitor. The deposited $ZnFe_2O_4$ nano-flakes thin film samples on FSSM substrates are designated as $ZnFe_2O_4$/FSSM-200, $ZnFe_2O_4$/FSSM-250 and $ZnFe_2O_4$/FSSM-300 for varying mesh size 200, 250 and 300 of FSSM, respectively. The investigation of the effect of mesh size on formation morphology of $ZnFe_2O_4$ nanostructures and their electrochemical performance for supercapacitor application is also carried out. Among the samples, $ZnFe_2O_4$/FSSM-300 demonstrated excellent pseudocapacitive behaviour with high specific capacitance (1625 F g^{-1} at 1 mA cm^{-2} current density), excellent cycle stability upto 8000 cycles with 97 % specific capacitance retention, which is marginally higher than $ZnFe_2O_4$/FSSM-250 (545 F g^{-1} at 1 mA cm^{-2} current density, 70 % retention), $ZnFe_2O_4$/FSSM-200 (241 F g^{-1} at 1 mA cm^{-2} current density, 56 % retention) and ferrite material based electrodes reported in literature (summarized in Table 1). Furthermore, the asymmetric pseudocapacitor device fabricated using $ZnFe_2O_4$/FSSM-300 as an anode and $Ni(OH)_2$/FSSM-300 as cathode also showed promising performance with high specific capacitance, justifying the significance and novelty of the work.

2. Experimental

2.1 Materials and Chemicals

FSSM substrate with different mesh size 200, 250 and 300 were purchased from Micro Mesh India Private Limited. The chemical reagents anhydrous zinc chloride ($ZnCl_2$), ferrous (II) chloride tetrahydrate ($FeCl_2.4H_2O$), monoethanolamine (MEA) and ammonia used for the synthesis were commercially procured from Merck chemicals. All the chemicals were used as received without further purification.

2.2 Synthesis of 3-D aligned and cross-linked $ZnFe_2O_4$ nano-flakes

In a typical synthesis, the bath solution was prepared by forming complex using 25 mL of 0.1 M $ZnCl_2$ solution and 3 mL MEA in 50 mL beaker. To this solution, 25 mL of freshly prepared 0.2 M $FeCl_2.4H_2O$ solution was added drop-wise with constant stirring while the stoichiometric ratio of metal precursors Zn:Fe (1:2) was maintained constant. This was followed by adding ammonia solution to adjust the pH at 9. On the other hand, the FSSM substrates of different mesh size (200, 250 and 300 mesh) were cut into 1 cm x 3 cm and ultrasonically cleaned in successive steps by soaking into detergent soap solution, distilled water and acetone for 30 min each. The pre-cleaned substrates were immersed carefully into the precursor bath solution, which was subsequently heated at temperature of 50 ^{o}C and the immersed substrates were rotated with gear motor of speed 55 rpm for 2.5 h. When the temperature reaches upto 35 ^{o}C, the bath reaction is established initiating nucleation and growth process. Same deposition procedure was adopted for growth of $ZnFe_2O_4$ nano-flakes on FSSM substrates with mesh size of 200 and 250 mesh. After completion of the deposition process, the deposited substrates were washed with double distilled water and dried overnight in oven at 60 ^{o}C. This was followed by annealing the samples at 450 ^{o}C in ambient air environment for 5 h.[43-45]

2.3 Material characterization

Scanning electron microscopy (SEM, JEOL JSM-6360), X-ray diffraction (XRD) (Bruker, D2-Phaser X-ray diffractometer) with $CuK_{\alpha 1}$ (λ =1.5406 Å) radiation in the range 20°-80°and Raman spectrometer (LabRAM HR) with 532 nm laser was used to characterize the morphology, crystal structure and phase identification of the samples. X-ray photoelectron spectroscopy (XPS) was carried out using an (XPS-PHI 5300 PHI USA) spectrometer. BET surface area analysis and pore size analysis was performed using Quantachrome NOVA1000e, USA.

2.4 Electrochemical measurements

All the electrochemical experiments were carried out in 6 M KOH aqueous electrolyte at room temperature using a CHI 608E electrochemical analyzer. Cyclic voltammetry (CV), galvanostatic charge-discharge (GCD) and electrochemical impedance spectroscopy (EIS) were carried out in a standard three-electrode system with graphite and a saturated Ag/AgCl electrode as the counter and reference electrodes. The $ZnFe_2O_4$/FSSM was used as the working electrode. The CV curves were measured under different scan rates of 10–100 mV s^{-1} between potential window -1.3 and 0 V. EIS measurements were carried out in the frequency range of 100 kHz to 1 Hz at an open circuit potential with an ac perturbation of 5 mV. The specific capacitance of the supercapacitor was calculated from the CV curves and GCD curves according to the following equations:[46, 47]

$$Csp = \frac{\int IdV}{v\times \Delta V\times m} \text{ -------------------------1}$$

$$Csp = \frac{I\times\Delta t}{\Delta V\times m} \text{ ---------------------------2}$$

Where I is the response current (mA cm^{-2}), m is the mass of the electrode (g), v is the potential scan rate (mV s^{-1}), and ΔV is the potential range (V).

2.5 Fabrication of an aqueous asymmetric supercapacitor

In the fabrication of thin film based asymmetric supercapacitor, the synthesized $ZnFe_2O_4$/FSSM-300 (2×2cm) was used as a negative electrode and $Ni(OH)_2$/FSSM-300 (2×2cm) was used as a positive electrode. The $Ni(OH)_2$ electrode was prepared by using reported CBD method.[48] These two electrodes were separated by a filter paper as a separator and soaked into 6 M KOH solution for about 24 h. Then, the device was encompassed between pair of glasses and insert into small bottle to avoid leakage of the electrolyte. The values of the specific capacitance, energy density and power density were based on the total mass of electrode material excluding the mass of FSSM. This mass was calculated by using simple weight difference method, wherein the value for negative electrode ($ZnFe_2O_4$/FSSM-300) was 0.5 mg, while for the positive electrode ($Ni(OH)_2$/FSSM-300) it was 0.3 mg.

3. Results and discussion

The vertically aligned and cross linked $ZnFe_2O_4$ nano-flakes structures on FSSM are reported for the first time and was obtained by rotational chemical bath deposition method (R-CBD) reported earlier.[43] Furthermore, in this work the effect of FSSM mesh size on morphology is also studied carefully. The formation mechanism of $ZnFe_2O_4$ thin films on FSSM (300 mesh) demonstrates cross linked nano-flakes structure as shown in Scheme 1.

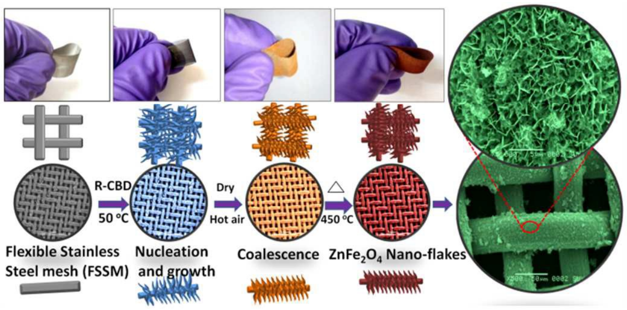

Scheme 1 Formation mechanism of $ZnFe_2O_4$ nano-flakes structure on FSSM

Fig. 1 presents scanning electron microscope (SEM) images of $ZnFe_2O_4$ nano-structures with different magnifications, grown on FSSM with different mesh size (200, 250 and 300) and represented as $ZnFe_2O_4$/FSSM-200, $ZnFe_2O_4$/FSSM-250 and $ZnFe_2O_4$/FSSM-300, respectively, obtained after annealing at 450 °C for 5h. The Fig. 1(a-a") shows SEM images of $ZnFe_2O_4$/FSSM-200 at different magnifications demonstrating network of $ZnFe_2O_4$ nano-sheets. The nano-sheet morphology is obtained due to the fast and free movement of the solution and molecules from within the 200 mesh (large size) enabling strong interaction on the surface of the substrate. When the mesh of FSSM was increased to 250 meshes (medium size), increased interaction of molecules during the rotation of substrates is obvious, which resulted in destruction of nano-sheets transforming them into nano-flakes like morphology of $ZnFe_2O_4$/FSSM-250 as shown in Fig. 1(b-b"). Interestingly, this observed destruction of nano-sheets transforming into nano-flakes increased our curiosity to investigate the effect of mesh size on morphology. The SEM images (Fig. 1(c-c")) obtained from FSSM-300 mesh showed formation of vertically aligned and cross linked $ZnFe_2O_4$ nano-flakes on the substrates. This nano-flake like morphology is obtained due to relatively slow and sluggish movement of the solution and molecules from within the 300 mesh (small size) enabling strong interaction on the surface of the rotating substrate.

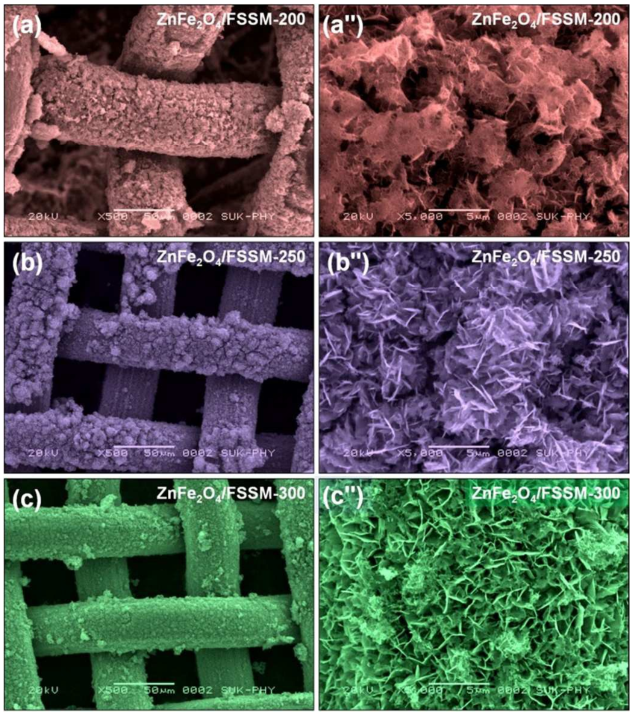

Fig. 1 Representative SEM images of (a-a") $ZnFe_2O_4$/FSSM-200, (b-b") $ZnFe_2O_4$/FSSM-250 and (c-c") $ZnFe_2O_4$/FSSM-300 mesh samples at x 500 and x5000 magnifications.

The crystal structure and phase formation was studied using XRD and Raman spectroscopy. The Fig. 2(a) presents the XRD patterns obtained from $ZnFe_2O_4$/FSSM-200, $ZnFe_2O_4$/FSSM-250 and $ZnFe_2O_4$/FSSM-300 samples. The peaks appearing at 2θ of 21.35°, 23.6°, 43.5° were assigned to SS (stainless steel) substrate, whereas, the diffraction peaks at 29.85° (220), 35.3° (311), 50.8° (400), 58.5° (511), 62.8° (440) and 74.7° (622) were attributed to the spinel cubic structure of $ZnFe_2O_4$ and is in good agreement with JCPDS card No.22-1012. The additional diffraction peak observed at 33° could be assigned to α-Fe_2O_3 formation due to unreacted FeOOH. To further investigate the crystal phase of $ZnFe_2O_4$ nano-flakes, Raman spectra of $ZnFe_2O_4$/FSSM-200, $ZnFe_2O_4$/FSSM-250 and $ZnFe_2O_4$/FSSM-300 mesh samples were recorded as shown in Fig.

2(b). The presence of four Raman active vibrational modes (A_{1g}+E_g+$2T_{2g}$) confirm the formation of $ZnFe_2O_4$ nano-flakes with cubic spinel phase and space group of Fd$\bar{3}$m. The peak corresponding to 666 cm^{-1} is attributed to A_{1g} symmetry is due to vibration of tetrahedral sites. The peaks at 223 and 463 cm^{-1} are attributed to T_{2g} symmetry and the peak at 351 cm^{-1} is assigned to E_g symmetry (vibrations of M-O octahedral sites).

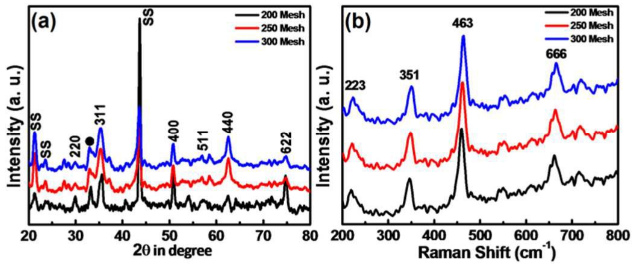

Fig. 2 Representative (a) XRD patterns and (b) Raman spectra of $ZnFe_2O_4$/FSSM-200, $ZnFe_2O_4$/FSSM-250 and $ZnFe_2O_4$/FSSM-300 mesh samples.

The elemental composition and chemical state of $ZnFe_2O_4$/FSSM-200, $ZnFe_2O_4$/FSSM-250 and $ZnFe_2O_4$/FSSM-300 mesh samples were investigated by X-ray photoelectron spectroscopy (XPS). Fig. 3(a) shows the XPS survey spectrum of $ZnFe_2O_4$ nano-flakes demonstrating the presence of Zn, Fe, O and C. The high resolution core level spectra of Zn_{2p} (Fig. 3(b)) showing two peaks around binding energy of 1022.25 and 1045.2 eV are assigned to $Zn_{2p3/2}$ and $Zn_{2p1/2}$. This indicates that the oxidation state of Zn in $ZnFe_2O_4$ nano-flakes is +2. Fig. 3(c) demonstrates the high resolution core level spectra Fe_{2p} showing the two peaks for $Fe_{2p3/2}$ and $Fe_{2p1/2}$ at binding energies of 725.5 and 711.7 eV, which confirms that the Fe in $ZnFe_2O_4$ exists in +3 oxidation state. The O1s core level spectra (Fig. 3(d)) shows one peak around 530.5 eV is mainly due the lattice O^{2-} in $ZnFe_2O_4$ nano-flakes. Binding energies of each thin film are found to be shifted in the decreasing order of $ZnFe_2O_4$/FSSM-300 > $ZnFe_2O_4$/FSSM-250 > $ZnFe_2O_4$/FSSM-200. This may be due to arrangement of vertically aligned interconnected morphology with maximum number of reaction sites as a result of mechanical force exerted with increasing mesh.

The pore structure and surface areas of $ZnFe_2O_4$/FSSM-200, $ZnFe_2O_4$/FSSM-250 and $ZnFe_2O_4$/FSSM-300 mesh samples were further characterized by nitrogen adsorption/desorption measurement and analyzed using the Barrett-Joyner-Halenda (BJH) and Brunauer-Emmett Teller (BET) methods.

The typical IV isotherms with type H4 hysteresis loops (Fig. 4(a)) confirm the formation of the open pores, generated from the decomposition of trapped MEA and the removal of water. The average pore diameter was calculated to be 4.5, 7.1 and 7.5 nm for $ZnFe_2O_4$/FSSM-300, $ZnFe_2O_4$/FSSM-250 and $ZnFe_2O_4$/FSSM-200 mesh samples, which are obtained from BJH plot (Fig. 4(b)). This result is consistent with the SEM observation. The BET specific surface area and pore volume of the $ZnFe_2O_4$/FSSM-300 was observed to be 54 m^2 g^{-1} and 0.1 cm^3 g^{-1}, respectively, which was higher than those obtained for $ZnFe_2O_4$/FSSM-250 (30 m^2 g^{-1} and 0.09 cm^3 g^{-1}) and $ZnFe_2O_4$/FSSM-200 (22 m^2 g^{-1} and 0.07 cm^3 g^{-1}) mesh, respectively. The large surface area and pore volume are essential for the electrode materials to achieve large specific capacitance as this reduces ion transport limitation in electrodes, ensuring full utilization of electrode materials.

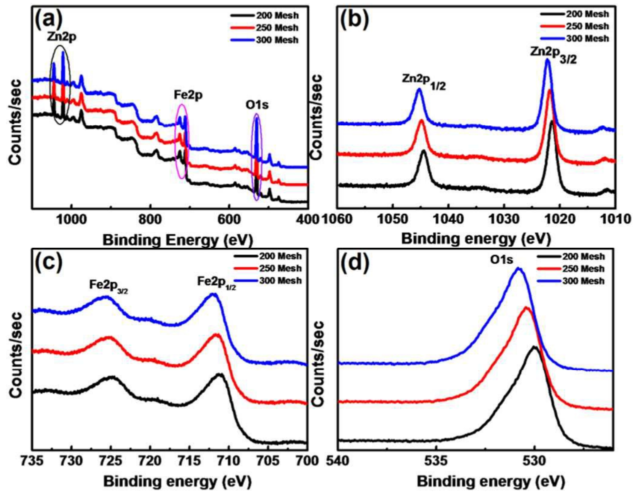

Fig. 3 (a) XPS survey spectra (b) Zn2p core level spectra (c) Fe2p core level spectra and (d) O1s core level spectra of $ZnFe_2O_4$/FSSM-200, $ZnFe_2O_4$/FSSM-250 and $ZnFe_2O_4$/FSSM-300 mesh samples.

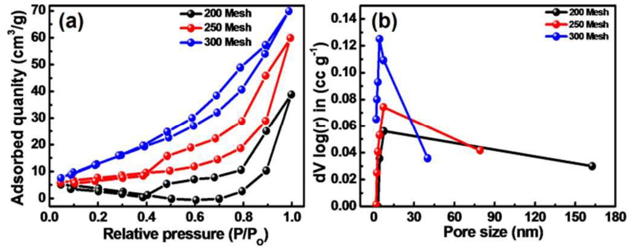

Fig. 4 (a) N_2-adsorption-desorption curves and (b) BJH pore size distribution of $ZnFe_2O_4$/FSSM-200, $ZnFe_2O_4$/FSSM-250 and $ZnFe_2O_4$/FSSM-300 mesh samples.

The porous nano-flaked $ZnFe_2O_4$/FSSM-200, $ZnFe_2O_4$/FSSM-250 and $ZnFe_2O_4$/FSSM-300 mesh electrode samples grown without the aid of binder and conductive agent were studied for their supercapacitor performances. All the electrochemical properties were carried out by constructing the cell of three electrode configuration in 6M KOH electrolyte. Fig. 5(a) presents the typical CV curves of the $ZnFe_2O_4$/FSSM-300 mesh sample electrode at various scan rates of 10-100 mVs^{-1} in the negative potential window ranging from -1.3 to 0.0 V (vs. Ag/AgCl). The shapes of the CV curves of all $ZnFe_2O_4$/FSSM-300 electrodes unambiguously demonstrate their pseudocapacitive characteristics. Especially, a pair of well-defined redox peaks could be found for all the three CV profiles of $ZnFe_2O_4$/FSSM-200 (Fig. S1(a)), $ZnFe_2O_4$/FSSM-250 (Fig. S1(b)) and $ZnFe_2O_4$/FSSM-300 (Fig. 5(a)) corresponding to the redox reaction between Fe(II) and Fe(III) associated with OH^- anion, which were distinguishable from those of electric double-layer capacitors, indicating the presence of a faradic reaction. Notably, the integral area of the CV profile for the $ZnFe_2O_4$/FSSM-300 electrode is observed to be higher than that of $ZnFe_2O_4$/FSSM-250 and

$ZnFe_2O_4$/FSSM-200 electrodes (see in ESI, Fig. S1(a) and S1(b)), indicating a significantly enhanced specific capacitance after the growth of vertically aligned and cross linked $ZnFe_2O_4$ nano-flakes on the surface of FSSM-300 mesh.

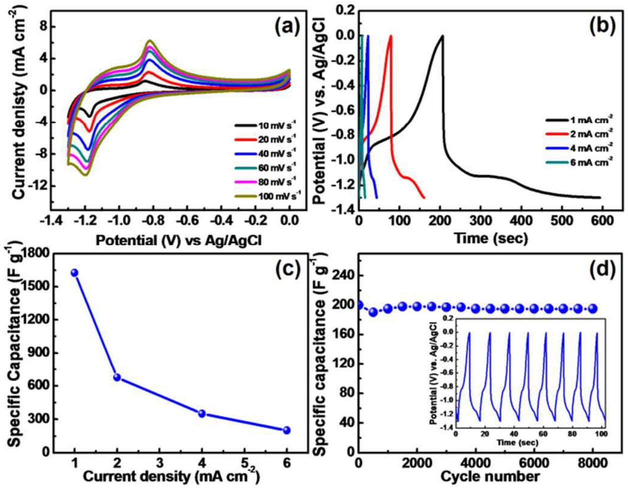

Fig. 5 (a) cyclic voltammogram (CV) at scan rates of 10-100 mV s^{-1}, (b) galvanostatic charge-discharge (GCD) measurements at different current densities of 1-6 mA cm^{-2}, (c) plot of specific capacitance (Csp) vs. Current density (CD) and (d) Cycle stability upto 8000 cycles and inset of first eight cycles of $ZnFe_2O_4$/FSSM-300 mesh sample.

The galvanostatic charge/discharge (GCD) curves of $ZnFe_2O_4$/FSSM-300 (Fig. 5(b)), $ZnFe_2O_4$/FSSM-250 (Fig. S1(c)) and $ZnFe_2O_4$/FSSM-200 mesh (Fig. S1(d)) samples at different current densities of 1-6 mA cm^{-2} show that the $ZnFe_2O_4$/FSSM-300 electrode has a longer discharge time (Fig. 5(b)), demonstrating relatively higher specific capacitance. FSSM has relatively good electrical conductivity and could facilitate the electron transfer during the charge/discharge process. Thus, the observed higher specific capacitance is probably due to the significant synergistic effect between FSSM-300 skeleton as a conductive core and vertically aligned and cross-linked $ZnFe_2O_4$ nano-flakes with high pseudocapacitance as a shell. The calculated specific capacitance of $ZnFe_2O_4$/FSSM-300 electrode in 6M KOH electrolyte are 1625, 675, 350 and 200 F g^{-1} obtained at current densities of 1, 2, 4 and 6 mA cm^{-2}, respectively. Fig. 5(c) shows the plot of specific capacitance with varying current densities for $ZnFe_2O_4$/FSSM-300 sample.

The specific capacitance values for $ZnFe_2O_4$/FSSM-300 are marginally higher than the values obtained for $ZnFe_2O_4$/FSSM-250 (545, 266, 216 and 125 F g^{-1}) and $ZnFe_2O_4$/FSSM-200 (241, 108, 50 and 13 F g^{-1}) at corresponding current densities of 1, 2, 4 and 6 mA cm^{-2}, respectively (See in ESI, Fig. S2(a)). The $ZnFe_2O_4$/FSSM-300 electrode was subjected to 8000 charging-discharging cycles at a current density of 5 mA cm^{-2} and it showed specific capacitance retention of 97 % (see Fig. 5(d)), while $ZnFe_2O_4$/FSSM-250 and $ZnFe_2O_4$/FSSM-200 electrode showed specific capacitance retention of 70% and 56%, respectively as shown in Fig. S2(b). The high capacity retention (97%) of the $ZnFe_2O_4$/FSSM-300 mesh samples electrode over 8000 cycles can be ascribed to the structure stability of the electrode material in the 6M KOH electrolyte. To further confirm the stability and quality of the $ZnFe_2O_4$/FSSM-300 electrode, SEM image of $ZnFe_2O_4$/FSSM-300 sample was recorded after the electrochemical cycle stability study for 8000 cycles. It was observed that there was no appreciable change in the morphology (Fig. S5; see in ESI) except for few sites showing agglomeration, probably due to deposition of electrolyte salts. Nevertheless, the porous structure of the $ZnFe_2O_4$ nano-flakes network was very well maintained. This demonstrates the long term stability of the electrode material. The supercapacitative performance of $ZnFe_2O_4$/FSSM-300 electrode was found to be promising when compared to $ZnFe_2O_4$/FSSM-250, $ZnFe_2O_4$/FSSM-200 electrodes and reported metal ferrite electrodes summarized in Table 1, and thus, $ZnFe_2O_4$/FSSM-300 electrode was used for fabrication of asymmetric supercapacitor (ASC) device and used for further studies.

Insert Table 1

The fabricated asymmetric supercapacitor (ASC) device involved use of $ZnFe_2O_4$/FSSM-300 as negative electrode and $Ni(OH)_2$/FSSM-300 as positive electrode in 6M KOH electrolyte. Based on the earlier literature reports it has been noticed that $Ni(OH)_2$ as an electrode material demonstrates higher specific capacitance and long cycle stability which are useful for storage of energy. Thus, $Ni(OH)_2$/FSSM-300 electrode as positive electrode is used in the present work. Study of the electrochemical properties of individual positive $Ni(OH)_2$/FSSM-300 electrode were performed as shown in Fig. S4 (ESI).

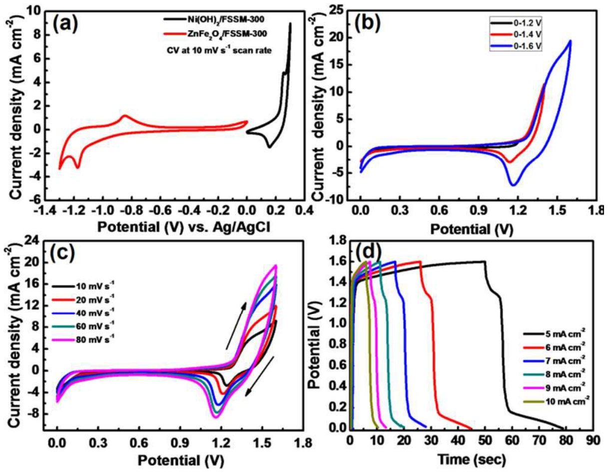

Fig. 6 Asymmetric pseudocapacitor device $ZnFe_2O_4$/FSSM-300||$Ni(OH)_2$/FSSM-300 performance (a) Cyclic voltammogram of negative ($ZnFe_2O_4$/FSSM-300) and positive ($Ni(OH)_2$/FSSM-300) electrodes at scan rates of 10 mV s^{-1} within potential range of -1.3 to 0.3 V. (b) Potential variation study from 0.0-1.2, 0.0-1.4 and 0.0-1.6 V at 80 mV s^{-1} scan rate. (c) CV curves at different scan rate of 10-80 mV s^{-1} and (d) GCD curves at different current densities of 5-10 mA cm^{-2}, respectively.

Fig. 6(a) shows the typical cyclic voltammograms of the individual negative electrode ($ZnFe_2O_4$/FSSM-300) and positive electrode ($Ni(OH)_2$/FSSM-300) at 10 mV s^{-1} in the potential range of -1.3 to 0V and 0 to 0.3 V, respectively, against Ag/AgCl electrode. Both the electrodes show redox pair in two different potential windows indicating the pseudocapacitive nature and hence the designed ASC was operated within the potential window of 0 to 1.6 V. Fig. 6(b) shows the cyclic voltammograms of the designed ASC recorded at a scan rate of 10 mV s^{-1} within potential window of 0 to 1.6 V. Fig. 6(c) shows the CV curves of the ASC plotted in the potential window of 0 to 1.6 V at varying scan rates (10-80 mV s^{-1}). It is observed from the CV plots shown in Fig. 6(b) and 6(c) that, the ASC could be operated till 1.6 V even with scan rate of 80 mV s^{-1}. However, during slow scan rates such as 10 and 20 mV s^{-1}, the current increases rapidly until it reach the breakdown point of electrolyte at the higher voltage window above 1.6 V. Therefore, for the sake of safety and long life of ASC, it is highly recommended to operate up to 1.6 V. All the CV plots were similar in shape, maintaining a pair of cathodic and anodic peaks. These redox peaks in the CV plots were found to shift away from each other with increasing scan rates. The redox peaks are indicative of the pseudocapacitive nature of ASC, which is clear from the large area of the corresponding CV plots. Charge-discharge (CD) curves of the ASC are shown in Fig. 6(d) and are recorded at current densities of 5, 6, 7, 8, 9 and 10 mA cm^{-2} within the potential window of 0 to 1.6 V. The observed nonlinear CD plots in Fig. 6(d) were in good support for the observed fast and reversible redox peaks recorded in the CV plots Fig. 6(c). The specific capacitance (Csp), energy density (E) and power density (P) of the ASC (expressed in F g^{-1}, W h kg^{-1} and kW kg^{-1}, respectively) were calculated from CD curve according to the formulae:

$$\boldsymbol{E} = \frac{\boldsymbol{Csp \times \Delta V^2}}{\boldsymbol{7.2}} \text{ ------------------------------ } 3$$

$$\boldsymbol{P} = \frac{\boldsymbol{3.6 \times E}}{\boldsymbol{\Delta t}} \text{ ------------------------------- } 4$$

Where, E is the energy density, P is the power density, Δt is the discharging time, Csp is the specific capacitance and ΔV is the potential window. Specific capacitances at different current densities were calculated and plotted in Fig. 7(a). The highest value of specific capacitance, i.e., 118 F g^{-1}, was achieved at a current density of 5 mA cm^{-2} and showed gradual reduction in specific capacitance upto 31 F g^{-1} with increasing current density from 5 mA cm^{-2} to 10 mA cm^{-2}. The estimated specific capacitance, energy density and power density of the designed ASC was compared with the previously reported ASCs based on the different MFe_2O_4 structures as shown in Table 1. The Ragone plot of the ASC (E vs. P) is shown in Fig. 7(b). Inset in Fig. 7(b) shows the schematic of the ASC device fabrication along with actual photograph of the electrodes and working of the device. The cyclic stability of a supercapacitor determines its application in industry. Here, the designed ASC was subjected to 8000 galvanostatic charging-discharging cycles at a current density of 9 mA cm^{-2} and the capacitance retention of the ASC is plotted in Fig. 7(c). The last eleven cycles of the GCD curves are plotted in Fig. 7(d). It is found that ASC retains 83 % of its specific capacitance up to 8000 cycles demonstrating good capacitance retention.

The flexibility is one of the important properties for the identification of the mechanical strength and quality of the electrodes. Therefore, CV curves of the fabricated ASC device at 60 mV s^{-1} scan rate were recorded with varying degree of bending angles (0^{o}, 30 ^{o}, 60 ^{o}, 90 ^{o}, 120 ^{o} and 180 ^{o}) and bending times (50, 100, 200 times). The CV curves obtained from ASC device with varying degree of bending angles and the CV curves obtained from ASC device after different number of bending times showed similar profile with no significant change as shown in Fig.S3 (a) and (b) (see ESI). This data supports the excellent flexibility and quality of the electrodes employed in the ASC device.

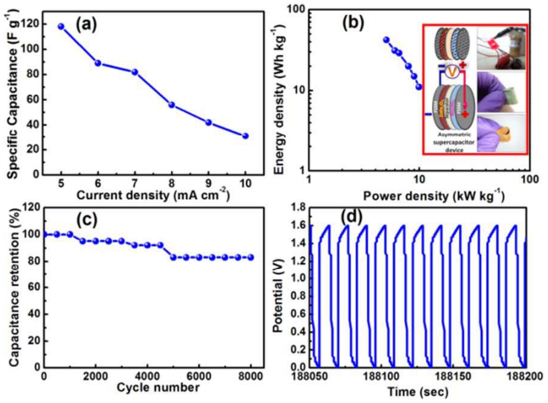

Fig. 7 (a) Specific capacitance (F g^{-1}) vs. Current density (mA cm^{-2}) (b) Ragone plot of energy density (Wh kg-1) vs. Power density (kW kg^{-1}) with inset of schematic construction of flexible $ZnFe_2O_4$/FSSM-300 thin film device (c) Cycle stability of device over 8000 cycles with 83% retention (d) Last 11 cycles of the asymmetric supercapacitor device.

Further evaluation of electrochemical performance was conducted by electrochemical impedance spectroscopy (EIS) for determining the internal resistance and charge transport of the ASC. Fig. 8(a) shows the Nyquist plot of the ASC in the frequency range of 100 kHz to 1 Hz with signal amplitude of 5 mV under open circuit potential (OCP). The inset of Fig. 8(a) also shows equivqlent circuit for the Nyquist plot in which R_{ct} is the charge transfer resistance, C_{dl} related with double layer capacitance, R_s is the equivalent series resistance (ESR) and w is Warburg impedance, respectively. The EIS plot can be easily distinguished into a small semicircle at the high frequency region and a straight line with a slope towards the low frequency region. The semicircle represents the charge transfer process and the sloped line represents the capacitive nature of the device.[49] The equivalent series resistance (ESR) could be estimated from the intercept at real impedance axis; it was found to be 3.0 ohm, which constitutes the resistance of the electrolyte, the resistance at electrode-electrolyte interface, the internal resistance of the electrode material and the contact resistance between the electrode and current collector. The diameter of the semicircle reveals the charge transfer resistance (R_{ct}), which is 1.0 ohm.

The large slope in the low frequency region of the Nyquist plot could be ascribed to the Warburg behavior, which arises from the fast ion diffusion across the electrode-electrolyte interface. Fig. 8(b) represent the Bode plots of phase angle and Bode plot of impedance against frequency for the ASC. The phase angle of 72^{o} at low frequency corresponds to capacitance contribution from pseudocapacitance. The frequency at which the maximum capacitance could be delivered is the response frequency (knee frequency) of the supercapacitor (f_0), which was found to be 3 Hz.

The response frequency divides the capacitive ($f < f_0$) and resistive ($f > f_0$) range of the supercapacitor. The corresponding relaxation time constant (or supercapacitor figure of merit, $\tau_o = 1/f_0$)[50] of the ASC was 0.3 s. The smaller time constant indicates the faster discharge of the entire stored energy of the supercapacitor, which justifies the observed higher power density of the ASC.[50]

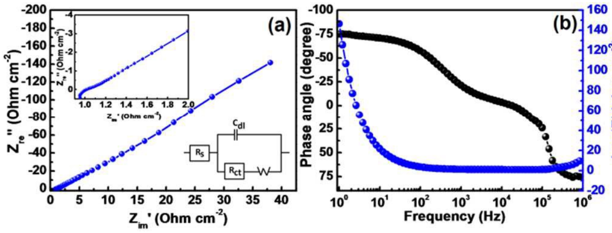

Fig. 8 (a) Nyquist plot with equivalent circuit (b) Bodes plots of the asymmetric supercapacitor device.

Conclusions

In summary, this works demonstrates a simple and cost-effective rotational chemical bath deposition method for the synthesis of 3-D aligned and cross linked $ZnFe_2O_4$ nano-flakes on flexible stainless steel mesh for the first time. The study of influence of FSSM (200, 250 and 300 mesh) on growth morphology of $ZnFe_2O_4$ nano-flakes and supercapacitative properties showed that $ZnFe_2O_4$/FSSM-300 demonstrates excellent morphology and improved supercapacitative properties (specific capacitance, energy density, cycle stability) which were marginally higher than $ZnFe_2O_4$/FSSM-200, $ZnFe_2O_4$/FSSM-250 and earlier reported MFe_2O_4 based electrode materials. Furthermore, the asymmetric pseudocapacitor device fabricated using $ZnFe_2O_4$/FSSM-300 as an anode and $Ni(OH)_2$/FSSM-300 as cathode showed remarkable performance with high specific capacitance (118 F g^{-1} at 5 mA cm^{-2}) and excellent cycle stability over 8000 cycles with 83 % capacitance retention. The device also delivered high energy density (42 Wh kg^{-1}) even at higher power density (5 kW kg^{-1}). The device was capable of demonstrating improved performance in the potential window of 0-1.6 V even at higher scan rates (80 mV s^{-1}). The stability and reversibility could be maintained at 1.6 V. The relaxation time constant of the ASC was estimated to be 0.3 s.

Acknowledgements

Authors MMV, SSK and AVG are thankful to UGC, UGC-SAP and DST-FIST, PURSE, New Delhi for financial support under UGC-BSR Meritorious Students fellowship and instrument facilities at the Department of Chemistry, Shivaji University, Kolhapur.

Notes and references

1. C. Liu, F. Li, L.-P. Ma and H.-M. Cheng, *Adv. Mater.,* 2010, **22,** E28-E62.
2. Z. Chang, Y. Yang, M. Li, X. Wang and Y. Wu, *J. Mater. Chem. A,* 2014, **2,** 10739-10755.
3. A. L. M. Reddy, S. R. Gowda, M. M. Shaijumon and P. M. Ajayan, *Adv. Mater.,* 2012, **24,** 5045-5064.
4. Y. Shi, L. Peng, Y. Ding, Y. Zhao and G. Yu, *Chem. Soc. Rev.,* 2015, , DOI: 10.1039/C5CS00362H.
5. Z. Wu, Y. Zhu and X. Ji, *J. Mater. Chem. A,* 2014, **2,** 14759-14772.
6. N. Linares, A. M. Silvestre-Albero, E. Serrano, J. Silvestre-Albero and J. Garcia-Martinez, *Chem. Soc. Rev.,* 2014, **43,** 7681-7717.
7. P. Simon and Y. Gogotsi, *Nat Mater,* 2008, **7,** 845-854.
8. Z.-S. Wu, W. Ren, L. Wen, L. Gao, J. Zhao, Z. Chen, G. Zhou, F. Li and H.-M. Cheng, *ACS Nano,* 2010, **4,** 3187-3194.
9. X.-l. Huang, D. Xu, S. Yuan, D.-l. Ma, S. Wang, H.-y. Zheng and X.-b. Zhang, *Adv. Mater.,* 2014, **26,** 7264-7270.
10. Z. Fan, J. Yan, T. Wei, L. Zhi, G. Ning, T. Li and F. Wei, *Adv. Funct. Mater.,* 2011, **21,** 2366-2375.
11. M. D. Stoller, S. Park, Y. Zhu, J. An and R. S. Ruoff, *Nano Lett.,* 2008, **8,** 3498-3502.
12. Y. Zhang, L. Li, H. Su, W. Huang and X. Dong, *J. Mater. Chem. A,* 2015, **3,** 43-59.
13. D. Yu, Q. Qian, L. Wei, W. Jiang, K. Goh, J. Wei, J. Zhang and Y. Chen, *Chem. Soc. Rev.,* 2015, **44,** 647-662.
14. L. L. Zhang and X. S. Zhao, *Chem. Soc. Rev.,* 2009, **38,** 2520-2531.
15. Y. Zhu, S. Murali, M. D. Stoller, K. J. Ganesh, W. Cai, P. J. Ferreira, A. Pirkle, R. M. Wallace, K. A. Cychosz, M. Thommes, D. Su, E. A. Stach and R. S. Ruoff, *Science,* 2011, **332,** 1537-1541.
16. V. Subramanian, C. Luo, A. M. Stephan, K. S. Nahm, S. Thomas and B. Wei, *J. Phys. Chem. C,* 2007, **111,** 7527-7531.
17. P.-C. Chen, G. Shen, Y. Shi, H. Chen and C. Zhou, *ACS Nano,* 2010, **4,** 4403-4411.
18. T. Nguyen, S. Eugenio, M. Boudard, L. Rapenne, M. J. Carmezim, T. M. Silva and M. F. Montemor, *Nanoscale,* 2015, **7,** 12452-12459.
19. K. Fukuda, T. Saida, J. Sato, M. Yonezawa, Y. Takasu and W. Sugimoto, *Inorg. Chem.,* 2010, **49,** 4391-4393.
20. H. Gao, F. Xiao, C. B. Ching and H. Duan, *ACS Appl. Mater. Interfaces,* 2012, **4,** 2801-2810.
21. F. Yang, M. Zhao, Q. Sun and Y. Qiao, *RSC Adv.,* 2015, **5,** 9843-9847.
22. C. Feng, J. Zhang, Y. He, C. Zhong, W. Hu, L. Liu and Y. Deng, *ACS Nano,* 2015, **9,** 1730-1739.
23. K. S. Yang, C. H. Kim and B.-H. Kim, *Electrochim. Acta,* 2015, **174,** 290-296.
24. X.-F. Lu, X.-Y. Chen, W. Zhou, Y.-X. Tong and G.-R. Li, *ACS Appl. Mater. Interfaces,* 2015, **7,** 14843-14850.
25. T. Huang, C. Zhao, R. Zheng, Y. Zhang and Z. Hu, *Ionics,* 2015, 1-7.
26. J. Cheng, Y. Lu, K. Qiu, H. Yan, X. Hou, J. Xu, L. Han, X. Liu, J.-K. Kim and Y. Luo, *Phys. Chem. Chem. Phys.,* 2015, **17,** 17016-17022.
27. Z. Wang, X. Zhang, Y. Li, Z. Liu and Z. Hao, *J. Mater. Chem. A,* 2013, **1,** 6393-6399.

28. M. Zhu, X. Zhang, Y. Zhou, C. Zhuo, J. Huang and S. Li, *RSC Adv.,* 2015, **5,** 39270-39277.
29. J. Yan, Q. Wang, T. Wei and Z. Fan, *Adv. Energy Mater.,* 2014, **4,** n/a-n/a.
30. P. Hao, Z. Zhao, L. Li, C.-C. Tuan, H. Li, Y. Sang, H. Jiang, C. P. Wong and H. Liu, *Nanoscale,* 2015, **7,** 14401-14412.
31. B. G. Choi, M. Yang, W. H. Hong, J. W. Choi and Y. S. Huh, *ACS Nano,* 2012, **6,** 4020-4028.
32. M. D. Stoller and R. S. Ruoff, *Energy Environ. Sci.,* 2010, **3,** 1294-1301.
33. D. Ling, N. Lee and T. Hyeon, *Acc. Chem. Res.,* 2015, **48,** 1276-1285.
34. S. Sharma, M. Tomar, N. K. Puri and V. Gupta, *Sensor. Actuator. A- Phys.,* 2015, **230,** 175-181.
35. J. W. Overcash and K. S. Suslick, *Chem. Mater.,* 2015, **27,** 3564-3567.
36. T. Liu, Y. Ling, Y. Yang, L. Finn, E. Collazo, T. Zhai, Y. Tong and Y. Li, *Nano Energy,* 2015, **12,** 169-177.
37. L. Han, Y. Cai, P. Tang and L. Zhang, *Mater. Today,* 2015, **18,** 410-411.
38. G. Nagaraju, Y. H. Ko and J. S. Yu, *J. Power Sources,* 2015, **283,** 251-259.
39. S. Liu, S. Sun and X.-Z. You, *Nanoscale,* 2014, **6,** 2037-2045.
40. R. Mandal, N. M. Hassan, J. Murimboh, C. L. Chakrabarti, M. H. Back, U. Rahayu and D. R. S. Lean, *Environ. Sci.Techn.,* 2002, **36,** 1477-1484.
41. J. S. Kim, S. S. Shin, H. S. Han, L. S. Oh, D. H. Kim, J.-H. Kim, K. S. Hong and J. Y. Kim, *ACS Appl. Mater. Interfaces,* 2014, **6,** 268-274.
42. S.-L. Chou, J.-Z. Wang, H.-K. Liu and S.-X. Dou, *J. Electrochem. Soc.,* 2008, **155,** A926-A929.
43. M. M. Vadiyar, S. C. Bhise, S. K. Patil, S. A. Patil, D. K. Pawar, A. V. Ghule, P. S. Patil and S. S. Kolekar, *RSC Adv.,* 2015, **5,** 45935-45942.
44. D. K. Pawar, J. S. Shaikh, B. S. Pawar, S. M. Pawar, P. S. Patil and S. S. Kolekar, *J. Porous Mater.,* 2012, **19,** 649-655.
45. V. S. Kumbhar, A. D. Jagadale, N. M. Shinde and C. D. Lokhande, *Appl. Surf. Sci.,* 2012, **259,** 39-43.
46. G. He, J. Li, W. Li, B. Li, N. Noor, K. Xu, J. Hu and I. P. Parkin, *J. Mater. Chem. A,* 2015, **3,** 14272-14278.
47. S. Gao, F. Liao, S. Ma, L. Zhu and M. Shao, *J. Mater. Chem. A,* 2015, **3,** 16520-16527.
49. M. S. Kolathodi, M. Palei and T. S. Natarajan, *J. Mater. Chem. A,* 2015, **3,** 7513-7522.
50. L. Yuan, X.-H. Lu, X. Xiao, T. Zhai, J. Dai, F. Zhang, B. Hu, X. Wang, L. Gong, J. Chen, C. Hu, Y. Tong, J. Zhou and Z. L. Wang, *ACS Nano,* 2012, **6,** 656-661.
51. Z.-Y. Yu, L.-F. Chen and S.-H. Yu, *J. Mater. Chem. A,* 2014, **2,** 10889-10894.
52. M. K. Zate, S. F. Shaikh, V. V. Jadhav, S. D. Waghmare, D. Y. Ahn, R. S. Mane, S.-H. Han and O.-S. Joo, *J. Nanoeng. Nanomanufact.,* 2014, **4,** 93-97.
53. W. Zhang, B. Quan, C. Lee, S.-K. Park, X. Li, E. Choi, G. Diao and Y. Piao, *ACS Appl. Mater. Interfaces,* 2015, **7,** 2404-2414.

Table Caption

54. H. Nan, L. Yu, W. Ma, B. Geng and X. Zhang, *Dalton Trans.,* 2015, **44,** 9581-9587.
55. C. Fu, A. Mahadevegowda and P. S. Grant, *J. Mater. Chem. A,* 2015, **3,** 14245-14253.
56. X.-W. Hu, S. Liu, B.-T. Qu and X.-Z. You, *ACS Appl. Mater. Interfaces,* 2015, **7,** 9972-9981.
57. J. Hao, W. Yang, Z. Zhang, B. Lu, B. Zhang and J. Tang, *Electrochimica Acta,* 2015, **152,** 13-18.
58. A. Shanmugavani and R. K. Selvan, *RSC Adv.,* 2014, **4,** 27022-27029.

Table 1 Comparative performance of $ZnFe_2O_4$/FSSM-300 with Literature reported iron oxide based electrodes for supercapacitor applications.

Sr. No	Method and Material	Substrate	Nano-Structure	Electrolyte	Specific Capacitance	Current density	Energy density	Reference and year
1	$NiFe_2O_4$ thin films and hydrothermal	Carbon cloth	Nanocubes	6 M KOH 1M H_2SO_4	922 F g^{-1} 1135 F g^{-1}	2 mA cm^{-2}	2.07 mWh cm^{-3} Device value	2014[51]
2	$NiFe_2O_4$ thin film and spray	Stainless steel plate	Particles	1 M Na_2SO_3	202 F g^{-1}	2 mA cm^{-2}	-	2015[52]
3	$CuFe_2O_4$-graphene powder and solvothermal	Ni Foil	Nano Crystals	3M KOH	576.6 F g^{-1}	1 A g^{-1}	15.8 Wh kg^{-1} Device value	2015[53]
4	α-Fe_2O_3 thin film and wet chemical method	Fe foil	Spinous	1M Na_2SO_4	524.6 F g^{-1}	1 A g^{-1}	38.6 Wh kg^{-1} Device value	2015[54]
5	Fe_3O_4/C powder and hydrothermal	Stainless steel	Necklace	3M KOH	225 F g^{-1}	1 A g^{-1}	-	2015[55]
6	Co_3O_4/$ZnFe_2O_4$ powder and hydrothermal	Stainless steel mesh	Starfish shape	6M KOH	326 F g^{-1}	1 A g^{-1}	82.5 Wh kg^{-1} single electrode	2015[56]
7	$CoFe_2O_4$ thin film and hydrothermal	Nickel foam	Flower	1M KOH	768 F g^{-1}	6 A g^{-1}	115 Wh kg^{-1} single electrode	2015[57]
8	$ZnFe_2O_4$ powder and combustion method	Graphite	Spherical shape	2M NaOH	1235 F g^{-1}	1 mA cm^{-2}	33 Wh kg^{-1} Device value	2014[58]
9	$ZnFe_2O_4$ thin film and CBD method	Stainless steel plates	Nano-flakes	3M KOH	768 F g^{-1}	5 mA cm^{-2}	106 Wh kg^{-1} single electrode	2015[43]
11	**$ZnFe_2O_4$ thin film and CBD method**	**Flexible stainless steel mesh**	**Nano-flakes**	**6M KOH**	**1625 F g^{-1}**	**1 mA cm^{-2}**	**42 Wh kg^{-1} Device value**	**Present Work**

Graphical Abstract

Low Cost Flexible 3-D Aligned and Cross-linked Efficient $ZnFe_2O_4$ Nano-flakes Electrode on Stainless Steel Mesh for Asymmetric Supercapacitor

Madagonda M. Vadiyar,[a] Sagar C. Bhise,[a] Sanjay S. Kolekar,[a]* Jia-Yaw Chang, [b]* Kaustubh S. Ghule[c] and Anil V. Ghule[c]*

[a]*Analytical Chemistry and Material Science Research Laboratory, Department of Chemistry, Shivaji University, Kolhapur 416004, Maharashtra, India.*
E-mail: sskolekar@gmail.com
[b]*Department of Chemical Engineering, National Taiwan University of Science and Technology, Taipei 10607, Taiwan. E-mail: jychang@mail.ntust.edu.tw*
[c]*Green Nanotechnology Laboratory, Department of Chemistry, Shivaji University, Kolhapur 416004, Maharashtra, India. E-mail: anighule@gmail.com*

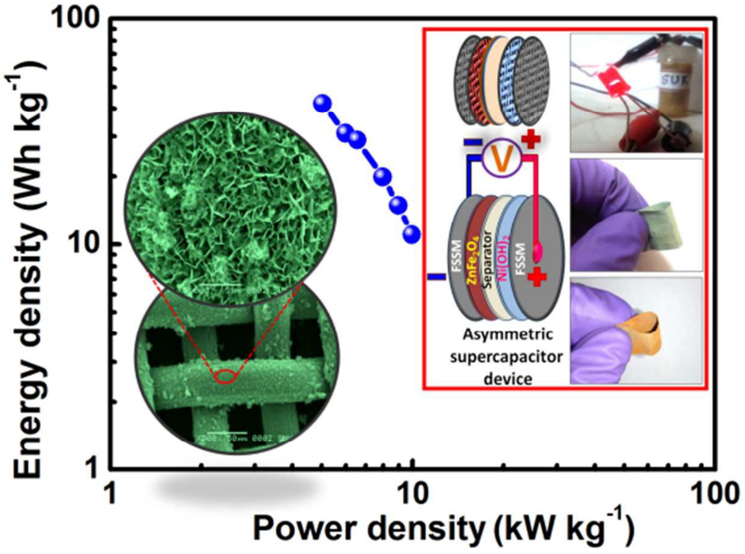

3-D $ZnFe_2O_4$/FSSM-300 nano-flakes on flexible stainless steel mesh as anode and $Ni(OH)_2$/FSSM-300 as cathode is used to fabricate asymmetric supercapacitor